

# Influence of copper ion doping on structural, optical and redox properties of CeO<sub>2</sub> nanoparticles

Anees A. Ansari<sup>1</sup> · J. Labis<sup>1</sup> · M. Alam<sup>2</sup> · Shahid M. Ramay<sup>3</sup> · N. Ahmad<sup>2</sup> · Asif Mahmood<sup>4</sup>

Received: 16 May 2015 / Accepted: 31 January 2016 / Published online: 20 February 2016  
© Springer Science+Business Media New York 2016

**Abstract** In this study, we doped different concentrations of copper ion in CeO<sub>2</sub> matrix to investigate the influence of doping concentrations on crystal structure, thermal, optical and redox properties of the as-prepared nanoproducts. X-ray diffraction (XRD) patterns indicate that the doped CeO<sub>2</sub> nanoparticles were highly crystalline with dominant (111) texture. No other impurities were observed and Cu ions were homogeneously distributed inside the CeO<sub>2</sub> lattice. As observed by transmission electron microscopy (TEM) the homogeneously distributed nanoparticles were agglomerated with increase doping contents because of decreased crystallinity. The temperature program reduction (TPR) technique was used to examine the redox character of the doped ceria nanoparticles. The Cu ions doped CeO<sub>2</sub> were reduced at low temperature indicating the high catalytic activity. The synergistic interaction between Cu and CeO<sub>2</sub> was the main factor responsible for high catalytic activity of the Cu doped CeO<sub>2</sub> model catalysts. Furthermore, the as-obtained Cu-doped CeO<sub>2</sub> nanoparticles revealed superior redox performance in contrast with pure CeO<sub>2</sub> prepared by the same route.

**Keywords** Ceria nanoparticles · Optical properties · Band gap energy · Redox properties

## 1 Introduction

In recent years, cerium oxides have attracted intensive attention of researchers due to their wide range of applications in various fields of material sciences as well as in biomedical sciences [1–4], such as ultraviolet (UV) absorbents [5] and for catalytic redox reactions in order to clean the exhaust of automobiles [6]. The catalytic effect of these materials comes from the reversible chemical reaction between the two cerium oxides; the oxygen-rich CeO<sub>2</sub> and the oxygen poor Ce<sub>2</sub>O<sub>3</sub>, depending on the chemical potential of oxygen [7–9]. For this reason, some studies on the electronic, bonding and optical properties of cerium oxide bulk crystals have been carried out from both fundamental and technology viewpoints [10–12]. Therefore, there is need to search for novel metal ions for doping in CeO<sub>2</sub> sub-lattice that enhance oxygen storage capacity and improve the catalytic activity of the ceria nanoparticles [6]. Many dopants such as transition metal ions, alkaline metals and rare-earth metal ions have been extensively used for doping in the Ce sub-lattice [6, 13–16]. Replacing Ce<sup>4+</sup> with +2 or +3 cations results in the creation of anion vacancy sites to compensate charges in the lattice. As a result, a solid electrolyte with predominantly ionic conductivity for oxygen over an extended temperature and oxygen partial pressure range may be produced [6, 7, 16]. Therefore, to induce higher conductivity, selection of dopant is very important, such that those dopants with the ionic radius close to that of matrix being are best suited. From this point of view transition metal ions are the likely candidates as dopants for CeO<sub>2</sub>. Previous research works in literature have shown that transition metal-containing nanocrystalline ceria are active and stable catalysts in low- and high-temperature redox reactions [6, 7, 16].

---

✉ Anees A. Ansari  
aneesaansari@gmail.com

<sup>1</sup> King Abdullah Institute for Nanotechnology, King Saud University, Riyadh -11451, Saudi Arabia

<sup>2</sup> Research Center, College of Science, King Saud University, P.O. Box 2455, Riyadh, Saudi Arabia

<sup>3</sup> Department of Physics, King Saud University, P.O. Box 2455, Riyadh, Saudi Arabia

<sup>4</sup> Department of Chemical Engineering, College of Engineering, King Saud University, Riyadh, Saudi Arabia

Among the transition metal ions doped CeO<sub>2</sub> nanoparticles systems examined in the literature, Cu ion doped CeO<sub>2</sub> is a particularly active and stable catalyst for low-temperature CO oxidation, methane oxidation, and the water gas shift reaction [6, 16]. Usually Cu metal ions doped CeO<sub>2</sub> nanoparticles have high specific surface areas and high oxygen storage capacities, which could highly improve the catalytic performance. Moreover, doped CeO<sub>2</sub> displays mixed conductivity (i.e. mixture of ionic and electronic conductivity) at low oxygen partial pressure. In reducing atmospheres oxygen may be lost from the lattice, which results in the reduction of Ce<sup>4+</sup> to Ce<sup>3+</sup>, and thus generates electrical carriers, oxygen vacancies, and electrons. Therefore, both electronic and ionic conductivity are enhanced in a reduced atmosphere and mixed conductivity prevails.

Until now, there are numerous methods of synthesizing CeO<sub>2</sub> and transition metal ion -doped CeO<sub>2</sub> nanoparticles that have been employed such as hydrothermal/solvothermal, high-temperature calcinations/combustion, high energy mechanical milling/ball milling, surfactant-assisted approach/ $\mu$ -emulsion, sol-gel technique, chemical filing, microwave, complexation, precipitation and co-precipitation etc. [17–22]. The metal complexation method, a version of the sol-gel technology, is an effective method for production (at relatively mild conditions) of crystalline, stoichiometric, phase homogeneous oxides [1]. The method is based on the Pechini process consisting of formation (in ethylene glycol medium) of complex (es) of the respective metals with poly ethylene glycol [23]. As a result of a following reflux with heating, a metal complex is formed in which metal ions are mixed. Different approaches were applied for isolation of the formed complexes and further doped nanoparticles from the complex. Some conventional decomposition reagents have been used to obtain the homogeneous precipitation of the mixed oxide nanoparticles such as urea, thiourea, hexamethylenetetramine, triethanolamine, ammonia, oxalic acid and strong bases (KOH, NaOH) etc. Among conventional decomposition of metal complex with ammonia or oxalic acid, the homogeneous precipitation is a kinetically controlled method of synthesis, where the precipitant agent is generated in the cation solution as a result of the hydrolysis of a reagent or the combination between two reagents. This process gives rise to a uniform and homogeneous distribution of precipitant throughout the reaction medium. This method has also been applied for the synthesis of doped ceria solid solutions resulting in the production of nanoparticles with less than 25 nm average size. Recently, other metal oxides have been prepared by this method, and the special features observed were attributed to the small size of the particles [17–22].

The objective of this research is to gain a systematic understanding on the influence on morphological structure, optical, thermal and temperature based reduction after copper ion doping in ceria nanoparticles. The obtained products can be well dispersed without deposition for several days in polar

solvents, such as water, ethanol, and glycol for there were vast glycol hydroxyl groups attached on the surface of the particles. The water concentration in the reaction system has greatly influenced the morphology of the obtained ceria. It has been found that nearly cubic ceria clusters have been formed when a minimum quantity of water and ammonia were added in the original system. This paper describes the precipitates from homogeneous precipitation process using ammonia and their thermal change. The copper doped ceria nanoparticles were examined using X-ray diffraction (XRD), FE-TEM, EDX, thermal gravimetry analysis (TGA), UV-Vis, FT-infrared spectrometry (FTIR) and temperature program reduction methods. In this paper the redox properties of Cu-doped CeO<sub>2</sub> nanoparticles were also investigated by temperature program reduction method. The redox property has been studied as a function of temperature and hydrogen partial pressure.

## 2 Experimental

### 2.1 Materials and methods

Cerium nitrate (99.99 %, BDH Chemicals Ltd., England), copper nitrate (E-Merck, Germany) ethylene glycol, C<sub>2</sub>H<sub>5</sub>OH, NH<sub>4</sub>OH were used as starting materials without any further purification. The ultrapure de-ionized water was used for preparation of solutions (Milli-Q system, Millipore, Bedford, MA, USA). All other chemicals used were of reagent grade.

### 2.2 Preparation of Cu ion-doped cerium oxide nanoparticles

In a typical reaction, 0.2 M Ce(NO<sub>3</sub>)<sub>3</sub> · 6H<sub>2</sub>O (0.99, 0.97 and 0.94 mol%) was dissolved in 50 ml ethylene glycol and heated on hot plate upto 80 °C. Separately 0.2 M copper nitrate (0.01, 0.03 and 0.06 mol%) dissolved in ethylene glycol was added drop-wise in the forgoing reaction and kept whole solution with magnetic stirring on hotplate at 80 °C to obtain homogeneously mixing. Later this homogeneously mixed solution was transferred in a 250 -ml flask fitted with reflux condenser and hydrolyzed for 24 h. An amount of ammonia was added to the hydrolyzed solution and the precipitate was obtained. The obtained gray colored precipitate was centrifuged and washed several times with distilled water to remove excess amount of ammonium and nitrate ions and the obtained product was dried at 100 °C. The as-prepared samples were annealed at 400 °C in air for 2 h. We examined the systematic changes in the color of the cerium hydroxide precipitate. The color of the prepared cerium hydroxide precipitate has changed gradually from gray to yellow after being exposed to air, maybe due to the oxidation of peroxide Ce(OH)<sub>3</sub>OOH to Ce(OH)<sub>4</sub> by oxygen. This procedure was repeated for the synthesis and purification of different Cu-doped CeO<sub>2</sub> concentrations.

### 2.3 Characterization

The crystallinity of the powder samples were examined by X-ray diffraction (XRD) at room temperature with the use of Rigaku-Dmax 2500 diffractometer equipped with Cu  $K_{\alpha}$  ( $\lambda = 1.54056 \text{ \AA}$ ) radiations as X-ray source. Thermogravimetric analysis (TGA) was performed with TGA/DTA, Mettler Toledo AG, Analytical CH-8603, Schwerzenbach, Switzerland. The size and morphology of the samples were inspected using a field emission transmission electron microscope (FE-TEM) equipped with the EDX (FETEM, JEM-2100F, JEOL, Japan) operating at an accelerating voltage of 200 kV. EDX analysis was used to confirm the presence of the elements. The samples for TEM were prepared by depositing a drop of a colloidal ethanol solution of the powder sample onto a carbon-coated copper grid. The FTIR spectra were recorded on a Perkin-Elmer 580B IR spectrometer using KBr pellet technique in the range  $4000\text{--}400 \text{ cm}^{-1}$ . The UV/Vis absorption spectra were measured in the Perkin-Elmer Lambda-40 spectrophotometer in the range  $200\text{--}600 \text{ nm}$ , with the sample contained in  $1 \text{ cm}^3$  stoppered quartz cell of  $1 \text{ cm}$  path length. Temperature programmed reduction by  $H_2$  ( $H_2$ -TPR) was performed on a Thermo-Finnigan TPDRO 1100 instrument with a thermal conductivity detector (TCD). Before detection, the gas was purified by a solid trap containing  $CaO + NaOH$  materials in order to remove the  $H_2O$  and  $CO_2$ . The quartz tube reactor was loaded with  $50 \text{ mg}$  sample in powder form and heated from room temperature to  $900 \text{ }^\circ\text{C}$  in  $5 \text{ \% } H_2/N_2$  mixture with a flow rate of  $20 \text{ ml min}^{-1}$ . By replacing the  $5 \text{ \% } H_2/N_2$  with  $5 \text{ \% } CO/He$ , the  $CO$ -TPR tests were also carried out. After the sample was reduced by  $5 \text{ \% } H_2/N_2$  from room temperature to  $500 \text{ }^\circ\text{C}$  and held for  $10 \text{ min}$ , temperature programmed oxidation (TPO) tests were performed from room temperature to  $900 \text{ }^\circ\text{C}$  in  $6 \text{ \% } O_2/He$  flow at a rate of  $20 \text{ ml min}^{-1}$ . All measurements were performed at room temperature.

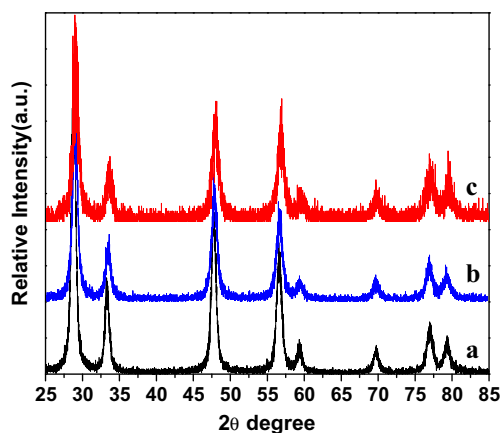


**Fig. 1** X-ray diffraction pattern of (a)  $CeO_2:Cu1\%$  (b)  $CeO_2:Cu3\%$  and (c)  $CeO_2:Cu6\%$  nanoparticles

### 3 Results and discussion

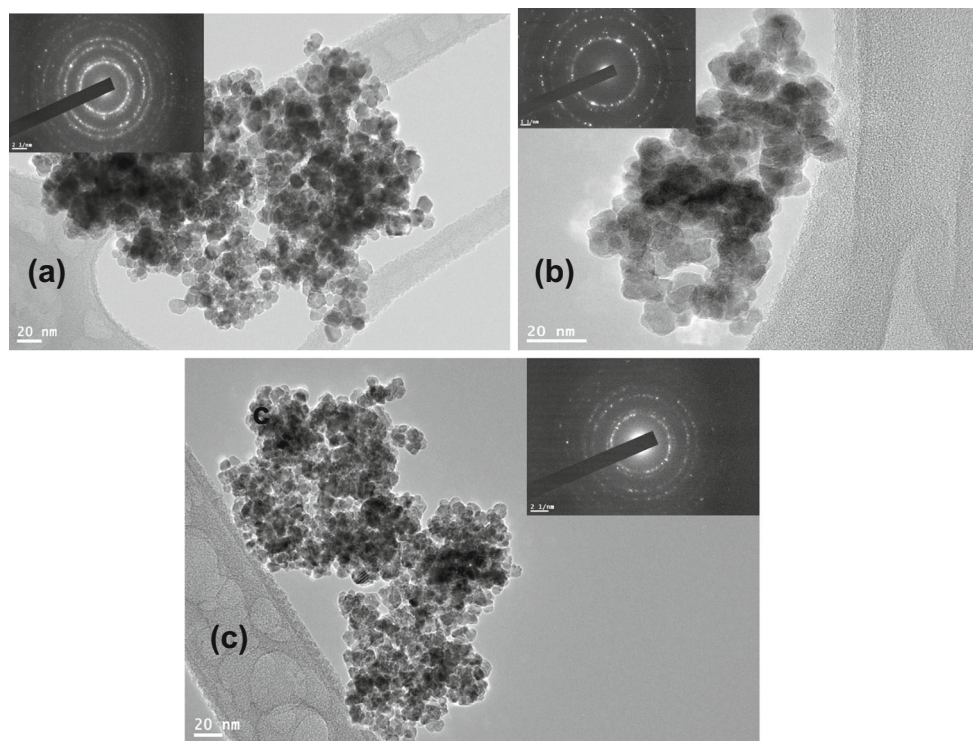
A representative XRD pattern of the synthesized Cu ion-doped  $CeO_2$  nanoparticles obtained is shown in Fig. 1. It can be observed, that all XRD reflection peaks correspond to the (111), (200), (220), (311) and (222) planes, which are well indexed and identified to the pure  $CeO_2$  nano-product (space group:  $Fm\bar{3}m$ ) and has the cubic fluorite phase (JCPDS card 12-0797) [22]. The peak positions and intensities of the reflection planes are in good agreement with the literature reports [15–22]. The broad diffraction peaks reflecting that the prepared products are in small grain size with high crystallinity [15, 21]. Absence of impurity peaks indicates good incorporation of Cu into the lattice sites of  $CeO_2$  or amount of compound too small to be detected by XRD. The structure of the copper-doped ceria remains the same upon doping, which suggests the formation of homogeneous Ce–Cu–O solid solutions [6]. The calculated average grain size as estimated from Scherrer formula for the Cu-doped  $CeO_2$  is 12.4, 10.4 and  $10.4 \text{ nm}$  for 1, 3 and 6 mol%, respectively. It can be observed that the reduction in the particle size leads to an increase in the lattice parameter.

The lattice constant of all samples were measured by fitting the peaks using Reitvald software (version 4.0). The estimated lattice parameter for the obtained product is found to be (i)  $5.4119 \pm 0.0043$  (ii)  $5.4118 \pm 0.0048$  (iii)  $5.4118 \pm 0.0046 \text{ \AA}$  respectively, which are slightly higher than its bulk counterpart ( $5.411 \text{ \AA}$ ) [22, 24]. This means that doping affects the crystal structure of nanoceria.  $CeO_2$  crystallizes in the fluorite structure, in which  $Ce^{4+}$  cation is surrounded by eight equivalent  $O^{2-}$  ions forming the corner of a cube, with each  $O^{2-}$  coordinated to four  $Ce^{4+}$  as reported in the literature [22, 25]. Due to the small ionic size of  $Ce^{4+}$  with respect to  $Ce^{3+}$ , the coordination number is reduced from eight to seven and  $Ce^{3+}$  ions is then introduced into the crystal lattice which has distorted the crystal structure. The introduction of oxygen vacancies with accompanying  $Ce^{3+}$  ions leads to a distortion of the local symmetry. This causes the change in the Ce–O bond length (lattice distortion) and the overall lattice parameter. Zou et al. suggested that the variation in the lattice parameter occurs due to the surface stress on  $CeO_2$  crystals [26]. The larger lattice parameter in nanocrystalline ceria implies that the migration enthalpy of an oxygen vacancy is smaller, resulting in a higher ionic conductivity and more efficient fuel cells. The systematic increase in lattice parameter with decreasing particle size provides specific control of the surface oxygen spacing and thus impact ceria catalysis of the water–gas shift and three-way auto exhaust clean-up reactions [27, 28].

#### 3.1 Tem/EDX

Figure 2 exhibits the FE-TEM micrographs of the prepared Cu-doped  $CeO_2$  nanoparticles at different doping concentrations. A high-magnification TEM image of the doped

**Fig. 2** FE-TEM micrographs of the as-prepared (a) CeO<sub>2</sub>:Cu1% (b) CeO<sub>2</sub>:Cu3% and (c) CeO<sub>2</sub>:Cu6% nanoparticles and inset of the images show the selected area electron diffraction pattern



nanoparticles shows that they exhibited a cross-lattice pattern, which demonstrates highly crystalline nature of the nanocrystals in a spherical morphology. It can be observed that most of them exhibit lattice fringes at distances of about 0.3 nm that well correspond to the (111) lattice plane of a fluorite-like cubic structure. The nanocrystallinity and crystallography of the as-prepared product are examined by selected area electron diffraction (SAED) analysis. The corresponding SAED pattern, as shown in the inset of Fig. 2, exhibits four broad rings with  $d$ -spacings of about 0.31, 0.27, 0.19 and 0.16 nm. Which could be attributed to (111), (200), (220) and (311) reflections of the fluorite cubic ceria structure, respectively.

The EDX graph shown in Fig. 3 confirms the presence of cerium (Ce), copper (Cu) and oxygen (O) in all Cu -doped CeO<sub>2</sub> nanoparticles. It should be noted that the origin of strong Cu and C peaks that appeared in the EDX spectra are from the carbon-coated Cu grid. So that it is difficult to differentiate the concentration of doped Cu peak in the EDX graphs. Also, no other impurities are evident in the figure implying that the doped nanoparticles are pure in chemical composition. This further confirms the phase purity of the synthesized Cu -doped CeO<sub>2</sub> nanoparticles.

#### 4 TGA/DTA

Comparative thermo-gravimetric analysis of Cu<sup>2+</sup> doped CeO<sub>2</sub> temperature nanoparticles under nitrogen with heating rate at

10 °C/min was carried out from ambient to 800 °C. The comparative thermal analysis of the doped metal oxide nanoparticles shows remarkable thermal stability, which was also confirmed by XRD analysis. The thermograms of the three doped nanoparticles are closely similar, showing two stepwise decompositions. As seen in Fig. 4(a,b and c), a weak endothermic peak before 200 °C, which is due to the evaporation of small amount of absorbed crystalline water or organic moiety in different bonding state for the present complex precursor system. In the second decomposition step, a sluggish weight loss was observed in all three thermograms from 200 to 800 °C. The slight difference in phase transition may be due to difference in duration of annealing at a particular temperature.

#### 5 FTIR

The FTIR spectra of the prepared Cu -doped CeO<sub>2</sub> nanoproductions shown in Fig. 5 reveals a diffused stretching vibrational band at round 3441 cm<sup>-1</sup> and weak bending vibrational bands at 1625, 1327 and 1062 cm<sup>-1</sup>. In lights of the proposed assignments of such peaks in other similar systems [29], the observed bands can be assigned to the broad band at 3441 and 1625 cm<sup>-1</sup> corresponding to the  $\nu$ (O–H) mode of (H-bonded) water molecules, and  $\delta$ (OH), respectively. The detection of hydroxyl groups indicates the presence of residual water molecules on the surface of Cu -doped CeO<sub>2</sub> nanoparticles. These results are in agreement with the TGA analysis.



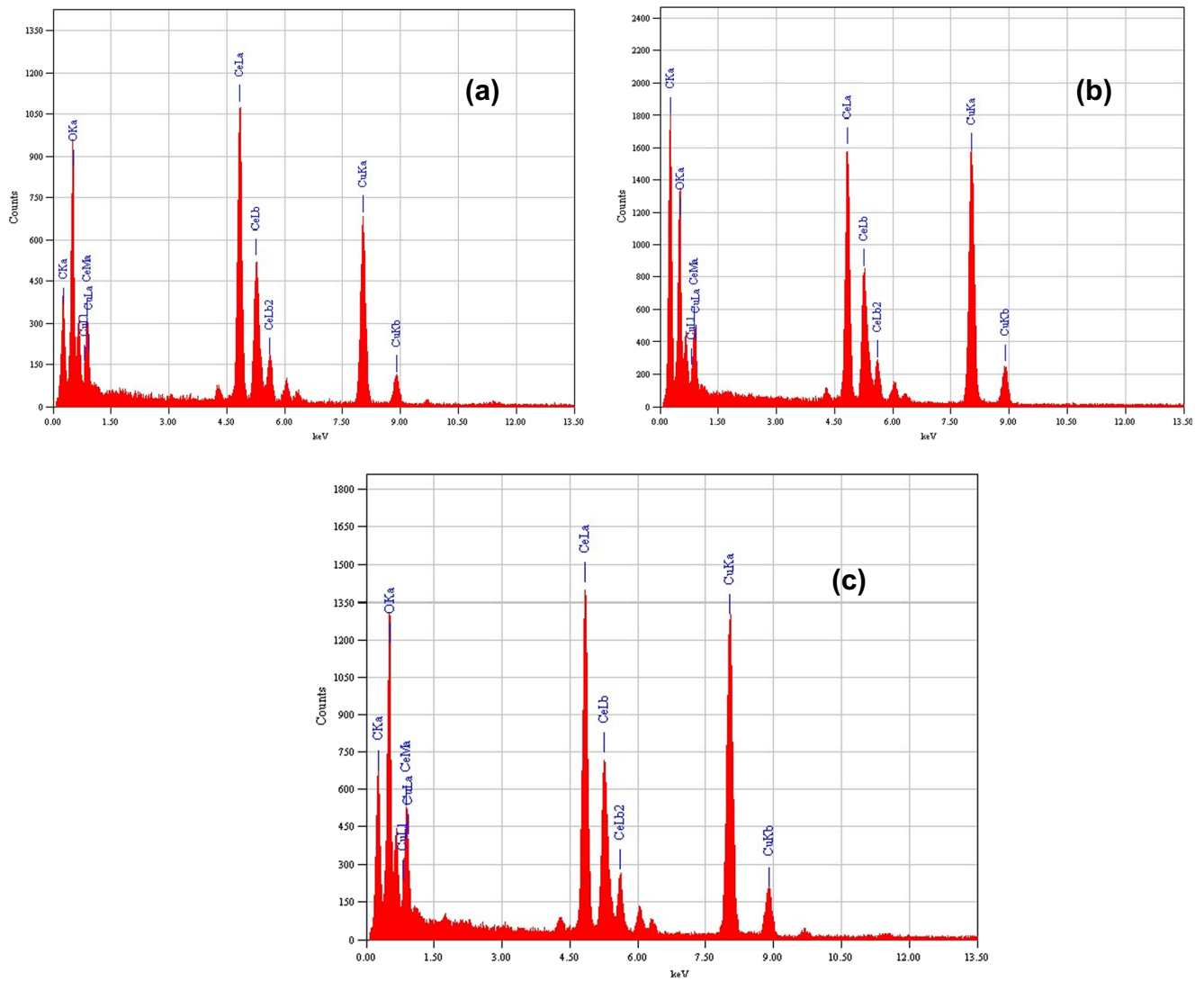


**Fig. 3** EDX analysis of the as-prepared (a) CeO<sub>2</sub>:Cu1% (b) CeO<sub>2</sub>:Cu3% and (c) CeO<sub>2</sub>: Cu6% nanoparticles

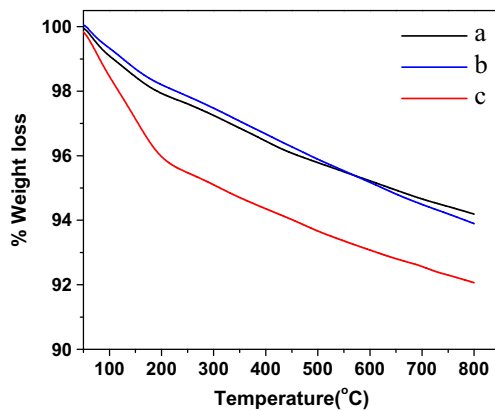


**Fig. 4** Thermo-gravimetric analysis of (a) CeO<sub>2</sub>:Cu1% (b) CeO<sub>2</sub>:Cu3% and (c) CeO<sub>2</sub>: Cu6% nanoparticles

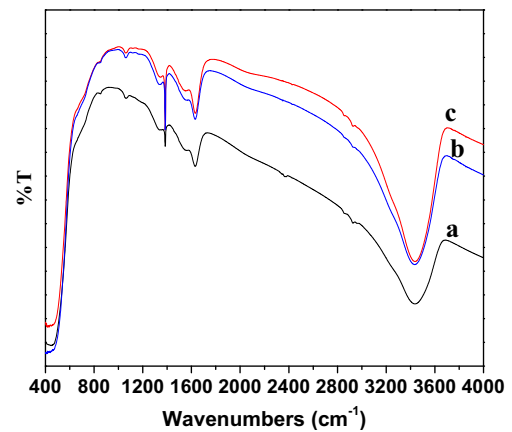


**Fig. 5** FTIR spectra of (a) CeO<sub>2</sub>:Cu1% (b) CeO<sub>2</sub>:Cu3% and (c) CeO<sub>2</sub>: Cu6% nanoparticles

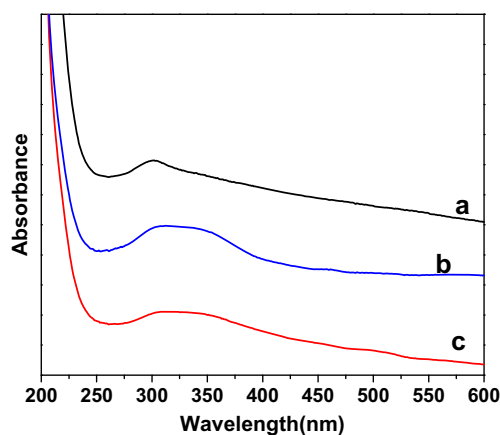


**Fig. 6** UV-vis absorption spectra of (a) CeO<sub>2</sub>:Cu1% (b) CeO<sub>2</sub>:Cu3% and (c) CeO<sub>2</sub>: Cu6% nanoparticles suspended in ethanol

The appearance of a sharp and intense band at 485 cm<sup>-1</sup> is assigned to the Ce-O-Cu stretching vibration mode [21, 29].

### 5.1 UV/Vis & Bandgap

Figure 6 shows the optical absorption spectra of different Cu ion concentration doped CeO<sub>2</sub> nanoparticles. A strong absorption band below 400 nm is observed in the spectra, which is due to the charge-transfer transition from O<sup>2-</sup> (2p) to Ce<sup>4+</sup> (4f) orbitals in CeO<sub>2</sub> [21, 30]. The absorption edge of 1 mol% Cu ion doped CeO<sub>2</sub> the doped nanomaterials gradually shifts toward longer wavelength indicating that the 3d transition metals supply lower unoccupied orbits than Ce 4 f. Thus the transition from O<sup>2-</sup> (2p) to the unoccupied orbits needs lower energy. The reason for the enhanced performance in the case of doped CeO<sub>2</sub> is due to the fact that the addition of Cu ions results in the formation of interstitial sites which in turn create new energy levels (impurity energy levels) between the valence and conduction bands [30]. The impurity energy levels allow for intrinsic band gap excitation under visible light region, and this implies that the higher energy state of 3d-electrons from Cu-cation dopants can be excited to the conduction band of CeO<sub>2</sub>, thereby enhancing its photocatalytic performance [31–35]. Consequently, it is proposed that the new absorption could induced by localizing the dopant level near the conduction band of CeO<sub>2</sub>. This kind of red shifting phenomenon in absorption spectrum of doped CeO<sub>2</sub> nanomaterial has been discussed in literature by many investigators [17–22] According to the absorption spectra, the optical band gaps ( $E_g$ ) of different Cu ion doped CeO<sub>2</sub> nanocrystals can be estimated by using the following equation:

$$(\alpha h\nu)^n = B (h\nu - E_g),$$

where  $h\nu$  is the photo energy,  $\alpha$  is the absorption coefficient, B is a constant relative to the material, and n is either two for a direct transition or 1/2 for an indirect transition. The curve of

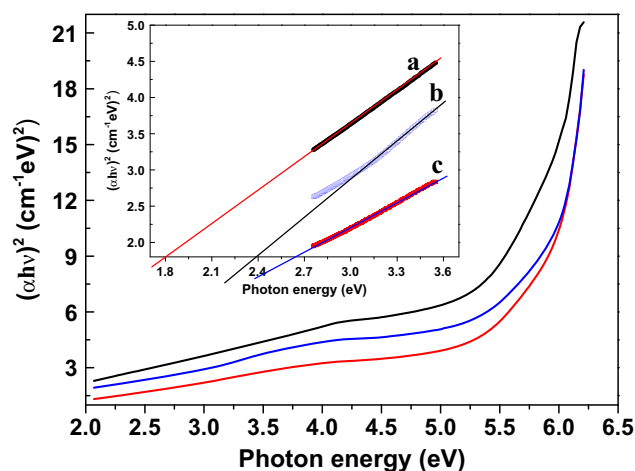


**Fig. 7** The plot of  $(\alpha h\nu)^2$  vs. photon energy( $h\nu$ ) of the (a) CeO<sub>2</sub>:Cu1% (b) CeO<sub>2</sub>:Cu3% and (c) CeO<sub>2</sub>: Cu6% nanoparticles

$(\alpha h\nu)^2$  versus  $h\nu$  for the samples is shown in Fig. 7. The correlated band gaps are 1.80, 2.38 and 2.63 eV for the 1, 3 and 6 mol% Cu ion doped CeO<sub>2</sub> nanoparticles, respectively. These are mostly lower than those of bulk powders (3.19 eV) due to the quantum-size effect [17–22, 30, 33–36]. These values are within the range reported in the literature. For example, Yue et al. have reported direct band gap values ranging from 2.69 to 2.81 eV for different transition metal ion doped CeO<sub>2</sub> nanoparticles synthesized using reverse co-precipitation method [37]. Some previous studies reported the quantum size effects in CeO<sub>2</sub> systems. Masui et al. reported band gaps of 4.1 and 2.6 nm CeO<sub>2</sub> nanoparticle prepared using reverse micelles to be 3.38 and 3.44 eV, respectively [36]. Yin et al. reported band gaps of 5.8 and 3.6 nm CeO<sub>2</sub> nanoparticles synthesized using sonochemical synthesis to be 3.03 and 3.68 eV, respectively [20]. Zhang et al. reported the increase in band gap by a value of 0.05 eV when the crystal size of CeO<sub>2</sub> nanoparticles was reduced from 6.9 to 4.6 nm [38]. In our work, the band

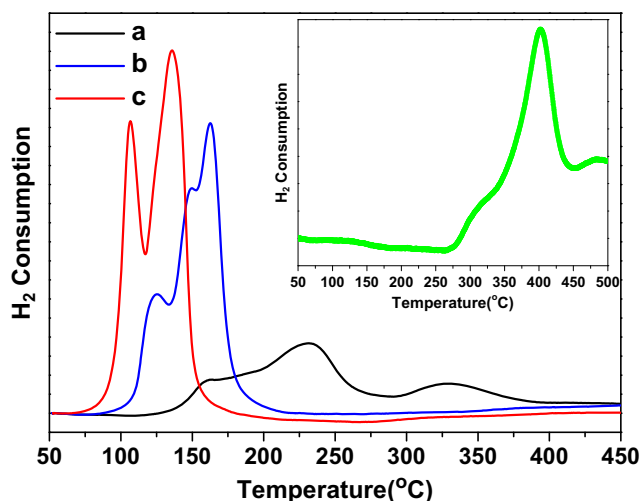


**Fig. 8** H<sub>2</sub>-TPR profiles of (a) CeO<sub>2</sub>:Cu1% (b) CeO<sub>2</sub>:Cu3% and (c) CeO<sub>2</sub>: Cu6% nanoparticles and inset shows the H<sub>2</sub>-TPR profile of pure CeO<sub>2</sub> nanoparticles

gaps were increased by 0.02 eV when the crystal size was decreased from 20 to 5 nm, indicating quantum confinement effect for our plate like CeO<sub>2</sub> nanoparticles [39].

## 5.2 Redox activity

The temperature-programmed reduction (TPR) technique was used to investigate the reducibility of the catalysts and determine the types of metal oxide species present in the various samples of copper metal ion doped cerium oxide nanoparticles. Here, the H<sub>2</sub>-TPR analysis (50–500 °C) was conducted on the prepared samples to reveal their redox properties. The TPR profiles are presented in Fig. 8. It can be seen that the profile of pure CeO<sub>2</sub> nanoparticles show two reduction peaks at 125 and 402 °C (inset Fig. 8), which can be attributed to the surface and bulk reduction of CeO<sub>2</sub> to Ce<sub>2</sub>O<sub>3</sub>, respectively [6]. After doping 1 mol% Cu ion into CeO<sub>2</sub> nanoparticles, two strong additional peaks at 200 and 230 °C were observed in the H<sub>2</sub>-TPR profile (Fig. 8a), which can be attributed to the reduction of well dispersed CuO species that strongly interact with the CeO<sub>2</sub> surface in the ceria lattice [6, 7]. Further increasing the copper content clearly resulted in reduction temperature at about 125 and 162 °C, which can be attributed to the reduction of Cu species, i.e., CuO → Cu<sub>2</sub>O and Cu<sub>2</sub>O → Cu<sup>0</sup>. The shift of the reduction peak to a lower temperature as the dopant cations were introduced indicates that the mobility of oxygen species is generally enhanced by the doping. [40, 41] This result demonstrates that the presence and quantity of Cu in CeO<sub>2</sub> determines the reducibility of the ceria. Furthermore, the reducibility character of ceria at low temperatures is suitable for catalyzing redox chemical reactions. It should also be noted that the intensity of the reduction peaks increases with increasing copper content. The enhancement of the peak area can be attributed to the synergistic effect between the dopants and cerium oxide through the formation of a Ce–Cu–O solid solution, which can create oxygen defects and structural distortion [40–42]. As more oxygen vacancies are produced, the surface oxygen concentration of the Cu-doped CeO<sub>2</sub> samples increases. This is consistent with the results of the Raman spectroscopic analysis [43]. No distinct reduction peaks due to copper oxide species were observed in 6 mol% doped CeO<sub>2</sub> nanoparticles indicating the formation of a complete solid solution of copper–cer peaks shifting the lower cerium oxide. The reduction peak for bulk CuO was reported at 320 °C [44]. The H<sub>2</sub>-TPR results for Cu confirm that strong synergistic interactions between Cu and Ce species facilitate the reduction of both copper and cerium [6]. The lowest reduction temperature and the largest reduction peak area indicate the excellent catalytic properties of copper-doped ceria. It is worth noting that the area of the reduction peak is related to the amount of H<sub>2</sub> consumed. On the basis of the peak areas in their TPR profiles, the three samples are shown with a sequence a ≥ b ≥ c, indicating their different catalytic properties. From the TPR profiles, it was observed that finely dispersed Cu–O was present in CeO<sub>2</sub>

nanoparticles, which could not be detected by XRD and the other techniques previously mentioned.

## 6 Conclusions

The doping of a transition metal in CeO<sub>2</sub> lattice remarkable affect physiochemical properties of the nanomaterials. The as-prepared nanoproducs consists of a narrow size -distribution of nanocrystalline Cu doped CeO<sub>2</sub> nanoparticles due to the use of a low dielectric constant reaction medium, responsible for reduced crystalline size. The band gap energies of the Cu doped CeO<sub>2</sub> nanoparticles increase with an increase in Cu dopant concentration indicating that increasing the dopant concentration induces formation of oxygen vacancies. These physiochemical properties and redox property based on temperature program reduction tests show that these doped ceria nanoparticles could have promising applications as electrode materials for electrochemical biosensor, solid oxide fuel cells and electrochromic devices, since they can be reduced at low temperature (about ~162 °C).

**Acknowledgements** The authors extend their sincere appreciations to the Deanship of Scientific Research at King Saud University for its funding this Prolific Research group (PRG-1436-26).

## References

1. J. Chen, S. Pati, S. Seal, J. F. McGinnis, *Nat. Nanotechnol.* **1**, 142 (2006)
2. J. Colon, L. Herrera, J. Smith, S. Patil, C. Komanski, P. Kupelian, S. Seal, D.W. Jenkins, C.H. Baker. *Nanomed.: Nanotech., Biol., and Med.* **5**, 225 (2009).
3. A. A. Ansari, P. R. Solanki, B. D. Malhotra, *J. Biotechnol.* **142**, 179 (2009)
4. A. A. Ansari, P. R. Solanki, B. D. Malhotra, *App. Phys. Lett.* **93**, 263901 (2008)
5. L. Liao, H. X. Mai, Q. Yuan, H. B. Lu, J. C. Li, C. Liu, C. H. Yan, Z. X. Shen, T. Y. J. *Phys. Chem. C* **112**, 9061 (2008)
6. H. Yen, Y. Seo, S. Kaliaguine, F. Kleitz, *Angew. Chem. Int. Ed.* **51**, 12032 (2012)
7. S. Mahammadunnisa, P. M. K. Reddy, N. Lingaiah, C. Subrahmanyam, *Catal. Sci. Technol.* **3**, 730 (2013)
8. S. Banerjee, P. S. Devi, D. Topwal, S. Mandal, K. Menon, *Adv. Funct. Mater.* **17**, 2847 (2007)
9. C. L. Robert, J. W. Long, K. A. Pettigrew, R. M. Stroud, D. R. Rolison, *Adv. Mater.* **19**, 1734 (2007)
10. T. Yu, J. Zeng, B. Lim, Y. Xia, *Adv. Mater.* **22**, 5188 (2010)
11. R. Si, Y. W. Zhang, L. P. You, C. H. Yan, *Angew. Chem., Int. Ed.* **44**, 3256 (2005)
12. T. Yu, J. Joo, Y. I. Park, T. Hyeon, *Angew. Chem., Int. Ed.* **44**, 7411 (2005)
13. A. A. Ansari, G. Sumana, M. K. Pandey, B. D. Malhotra, *J. of Mater. Res.* **24**, 1667 (2009)
14. A. A. Ansari, G. Sumana, R. Khan, B. D. Malhotra, *J. of Nanosci. & Nanotech.* **9**, 4679 (2009)
15. S. Patil, S. Seal, Y. Guo, A. Schulte, J. Norwood. *Appl. Phys. Lett.* **88**, 243110 (2006)

16. J. Zhang, J. Guo, W. Liu, S. Wang, A. Xie, X. Liu, J. Wang, Y. Yang, *Eur. J. Inorg. Chem.* 969 (2015)
17. H. I. Chen, H. Y. Chang, *Ceram. Intern.* **31**, 795 (2005)
18. J. J. Miaoa, H. Wanga, Y. R. Lia, J. M. Zhu, J. J. Zhu, *J. Crys. Growth* **281**, 525 (2005)
19. D.E. Zhang, X.J. Zhang, X.M. Ni, J.M. Song, H.G. Zheng. *Chem Phys chem*, **7**, 2468 (2006).
20. L. Yin, Y. Wang, G. Pang, Y. Kolytyn, A. Gedanken, *J. Coll. Inter. Sc.* **246**, 78 (2002)
21. A. A. Ansari, *J. Semicond.* **31**, 053001 (2010)
22. Z. Wang, Z. Quan, J. Lin, *Inorg. Chem.* **46**, 5237 (2007)
23. M. P. Pechini, US Patent **3**, 330697A (1967)
24. S. Babu, A. Schulte, S. Seal, *Appl. Phys. Lett.* **92**, 123112 (2008)
25. S. Deshpande, S. Patil, S. V. N. T. Kuchibhatla, S. Seal, *Appl. Phys. Lett.* **87**, 133113 (2005)
26. H. Zou, Y. S. Lin, N. Rane, T. He, *Ind. Eng. Chem. Res.* **43**, 3019 (2004)
27. A. Tschope, D. Schaadt, R. Birringer, J. Y. Ying, *Nanostruct. Mater.* **9**, 423 (1997)
28. F. Zhang, S. W. Chan, J. E. Spanier, E. Apak, Q. Jin, R. D. Robinson, I. P. Harman, *Appl. Phys. Lett.* **80**, 127 (2002)
29. A. A. Ansari, A. Kaushik, P. R. Solanki, B. D. Malhotra, *Electrochem. Commun.* **10**, 1246 (2008)
30. A. A. Ansari, S. P. Singh, B. D. Malhotra, *Journal of Alloy & Compounds* **509**, 262 (2011)
31. G. F. Zhang, G. Fang, L. L. Ping, G. S. Li, X. Q. Qiu, *Chin. J. Struc. Chem.* **29**, 307 (2010)
32. M. A. Khana, S. I. Woo, O. B. Yang, *Intern. J. Hydrogen. Energy* **33**, 5345 (2008)
33. K. Ahadi, A. Nemati, S. M. Mahdavi, A. Vaezi, *J. Mater. Sci.: Mater. Electron.* **24**, 2128 (2013)
34. K. Ahadi, A. Nemati, S. M. Mahdavi, *Mater. Lett.* **83**, 124 ((2012)
35. K. Ahadi, S. M. Mahdavi, A. Nemati, M. Kianinia, *J. Mater. Sci. Mater. Electron.* **22**, 815 (2011)
36. T. Masui, K. Fujiwara, K. Machida, G. Adachi, *Chem. Mater.* **9**, 2197 (1997)
37. L. Yue, X. M. Zhang, *J. Alloys Comp.* **475**, 702 (2009)
38. Y. W. Zhang, R. Si, C. S. Lia, C. H. Yan, C. X. Xiao, Y. Kou, *J. Phys. Chem. B* **107**, 10159 (2003)
39. S. Maensiri, C. Masingboon, P. Laokul, W. Jareonboon, V. Promarak, P. L. Anderson, S. Seraphin, *Crys. Growth & Design* **7**, 950 (2007)
40. J. Saranya, K. S. Ranjith, P. Saravanan, D. Mangalaraj, R. T. R. Kumar, *Mater. Sc. Semicond. Process.* **26**, 218 (2014)
41. H. F. Li, G. Z. Lu, Y. Q. Wang, Y. Guo, Y. L. Guo, *Catal. Commun.* **11**, 946 (2010)
42. B. M. Reddy, G. Thrimurthulu, L. Katta, Y. Yamada, S. E. Park, *J. Phys. Chem. C* **113**, 15882 (2009)
43. Z. D. D. Mitrovic, M. Radovic, M. Scepanovic, M. G. Brojcin, Z. V. Popovic, B. Matovic, S. Boskovic, *Appl. Phys. Lett.* **91**, 203118 (2007)
44. X. F. Yu, N. Z. Wu, Y. C. Xie, Y. Q. Tang, *J. Mater. Chem.* **10**, 1629 (2000)